





Article

Preparation of $\text{Ca}_2\text{Al}_{1-m}\text{Fe}_m(\text{OH})_6\text{Cl}\cdot 2\text{H}_2\text{O}$ -Doped Hydrocalumites and Application of Their Derived Mixed Oxides in the Photodegradation of Ibuprofen

Alejandro Jiménez ¹, Marta Valverde ¹, Alexander Misol ¹, Raquel Trujillano ¹, Antonio Gil ²
and Miguel Angel Vicente ^{1,*}

¹ Departamento de Química Inorgánica, GIR—QUESCAT, Universidad de Salamanca, E-37008 Salamanca, Spain

² INAMAT², Departamento de Ciencias, Edificio de los Acebos, Campus de Arrosadía, Universidad Pública de Navarra, E-31006 Pamplona, Spain

* Correspondence: mavicente@usal.es

Abstract: Aluminum from saline slags generated during the recycling of this metal, extracted under reflux conditions with aqueous NaOH, was used in the synthesis of hydrocalumite-type solids with the formula $\text{Ca}_2\text{Al}_{1-m}\text{Fe}_m(\text{OH})_6\text{Cl}\cdot 2\text{H}_2\text{O}$. The characterization of the obtained solids was carried out by powder X-ray diffraction, infrared spectroscopy, thermal analysis, element chemical analysis, N_2 adsorption-desorption at -196°C and electron microscopy. The results showed the formation of Layered Double Hydroxide-type compounds whose characteristics varied as the amount of incorporated Fe^{3+} increased. These solids were calcined at 400°C and evaluated for the catalytic photodegradation of ibuprofen, showing promising results in the elimination of this drug by advanced oxidation processes. The CaAl photocatalyst (without Fe) showed the best performance under UV light for the photodegradation of ibuprofen.

Keywords: hydrocalumite; aluminum saline slag recovery; photocatalysis; ibuprofen degradation



Citation: Jiménez, A.; Valverde, M.; Misol, A.; Trujillano, R.; Gil, A.; Vicente, M.A. Preparation of $\text{Ca}_2\text{Al}_{1-m}\text{Fe}_m(\text{OH})_6\text{Cl}\cdot 2\text{H}_2\text{O}$ -Doped Hydrocalumites and Application of Their Derived Mixed Oxides in the Photodegradation of Ibuprofen.

ChemEngineering **2022**, *6*, 64.
<https://doi.org/10.3390/chemengineering6040064>

Academic Editor: Alirio E. Rodrigues

Received: 5 July 2022

Accepted: 12 August 2022

Published: 18 August 2022

Publisher's Note: MDPI stays neutral with regard to jurisdictional claims in published maps and institutional affiliations.



Copyright: © 2022 by the authors. Licensee MDPI, Basel, Switzerland. This article is an open access article distributed under the terms and conditions of the Creative Commons Attribution (CC BY) license (<https://creativecommons.org/licenses/by/4.0/>).

1. Introduction

Technological progress in recent years requires the use of increasingly sophisticated materials for specific applications, and these materials must also be eco-friendly, avoiding as much as possible the generation of polluting wastes. Aluminum is the second most widely used metal in the world, after iron [1,2]. Its excellent properties make it an ideal material for various sectors such as military, machinery, aerospace, building or food [3–6]. The combination of the Bayer and Hall-Héroult processes allows for obtaining aluminum from natural bauxite, with the disadvantage of high electricity consumption and generation of several wastes, including *red mud*. This is known as *Primary Aluminum Production (PAP)* [2,4,6–10]. Another way to obtain it is *Secondary Aluminum Production* which is based on the recycling of the metal. In this case, the process requires less electricity consumption and the addition of salts (mainly NaCl and KCl) for melting the aluminum, generating an important residue, known as *Salt Cake* or *Saline Slags* [2,4,6–10]. According to the European Normative [11], salt cake is considered hazardous waste. Several valorization procedures were proposed, among which the following stand out: (a) its direct use as an adsorbent [12–14] or (b) extraction of aluminum [4,5,9] and its subsequent use in the preparation of Al^{3+} -based materials such as alumina [15], zeolites [7,16], or layered double hydroxides (LDHs) [8,17–20], among others.

LDHs are a family of compounds whose structure is derived from brucite ($\text{Mg}(\text{OH})_2$) and whose general formula is $[\text{M}(\text{II})_{1-x}\text{M}(\text{III})_x(\text{OH})_2]^{x+}[\text{A}_{x/n}]^{n-}\cdot m\text{H}_2\text{O}$ (M(II) and M(III) are divalent and trivalent cations and A is the interlayer anion) [21]. A large number of divalent cations (Ni, Co, Cu, Mg, Ca or Zn) form LDH with several trivalent cations

(Al, Fe, Cr, Y or Ga) [21], and the Li–Al LDH was also described [22,23]. Hydrocalumite, $\text{Ca}_2\text{Al}(\text{OH})_6\text{Cl}\cdot 2\text{H}_2\text{O}$, belongs to the LDH family [21]. Among its most important applications are: adsorbent [24], antacid [25], ion-exchanger [26], and basic heterogeneous catalyst [27–31]. We recently reported the preparation of hydrocalumite from saline slags [8].

Ibuprofen (IBU) is a non-steroidal drug widely used as an anti-inflammatory, antipyretic, and analgesic [32]. Its chemical structure consists of an alkylbenzene ring with a carboxylic acid functional group, whose pK_a is 4.8 [33]. The presence of IBU and other pharmaceuticals and personal care products (PPCP) in surface waters was reported by several authors, their elimination being not possible by classical biological treatments and including these drugs among the emerging pollutants [34–44].

Advanced oxidation processes (AOPs), especially heterogeneous photocatalysis, are presented as a promising technology for wastewater purification and treatment [36]. This methodology achieves the degradation and/or mineralization of pollutants. Photocatalysis, ozonation or the Fenton process are AOP [41]. Heterogeneous photocatalysis is a versatile and environmentally friendly technique based on the use of light and a photocatalyst. Light is used to activate the catalyst, which is a semiconductor that generates highly reactive radicals that degrade the pollutant [41]. The par-excellence photocatalyst is titanium dioxide (TiO_2), while zinc oxide (ZnO), iron (III) oxide (Fe_2O_3) or vanadium (V) oxide (V_2O_5) are also widely used [45–47]. The performance of the process can be improved by dispersing the photocatalyst on a support such as mixed metal oxides (MMO) [48,49]. In this sense, LDH can be excellent precursors of MMO by calcination through topological transformation [21,47,50]. Di et al. have recently reported that bifunctional ZnFe-MMOs prepared from LDH show high performance in IBU degradation under simulated solar irradiation [51].

Although the Fe–Al substitution in hydrocalumites should be expected, to the best of our knowledge, only a few works have explored the study of this type of LDH compound. Thus, Phillips and Vandeperre have investigated the adsorption of nitrate, chloride and carbonate by LDH-CaAlFe-type solids [52], while Lu et al. have applied these solids as heterogeneous catalysts in the production of biodiesel from soybean oil by transesterification reaction [53], and Szabados et al. have studied the preparation of LDH-CaAlFe by a combination of dry-milling and ultrasonic irradiation in aqueous solution [54]. Although some work was carried out using other LDH solids, mainly hydrotalcite-type (an LDH family similar to hydrocalumite), hydrocalumite solids are very scarcely used for investigating the degradation of emerging pollutants. Sánchez-Cantú et al. have used hydrocalumite-type compounds as catalyst precursors in the photodegradation of 2,4-dichlorophenoxyacetic acid [55]. Thus, in this work, hydrocalumites with the theoretical formula $\text{Ca}_2\text{Al}_{1-m}\text{Fe}_m(\text{OH})_6\text{Cl}\cdot 2\text{H}_2\text{O}$, incorporating variable amounts of Fe^{3+} , were prepared following the methodology recently reported by Jiménez et al. for the preparation of hydrocalumite from aluminum saline slags [8]. These CaAlFe hydrocalumites were calcined at 400 °C and the resulting solids were used in the removal of ibuprofen, evaluating their adsorption and catalytic photodegradation capacities. Therefore, this work can be framed within the circular economy, as waste from aluminum recycling was used to synthesize LDH-CaAlFe which, after being calcined at 400 °C, showed high efficiency in the removal of ibuprofen by means of an AOP.

2. Materials and Methods

2.1. Materials

Aluminum saline slag was kindly supplied by IDALSA (Ibérica de Aleaciones Ligeras S.L., Pradilla de Ebro, Zaragoza, Spain). NaOH (pharma grade), HCl (pharma grade, 37%) CaCl_2 (anhydrous, 95%), $\text{FeCl}_3\cdot 6\text{H}_2\text{O}$ (97–102%) were from Panreac, while $\text{CaCl}_2\cdot 2\text{H}_2\text{O}$ (ACS 99–105%) was supplied by Alfa Aesar and ibuprofen sodium salt (98%) was supplied by Sigma Aldrich, St. Louis, MO, USA. All were used as received, without any treatment.

2.2. Preparation of CaAlFe Mixed Metal Oxides

The methodology recently reported by some of us in [8] to prepare hydrocalumite was followed. Saline slags were ground and washed until obtaining a chloride-free solid, the fraction smaller than 0.4 mm was extracted with NaOH, as reported elsewhere [9], and the solution was treated with HCl to precipitate silicon-containing species as SiO₂; addition of CaCl₂·2H₂O and FeCl₃·6H₂O at pH 11.5 (fixed using NaOH) led to the formation of a precipitate, that was submitted to treatment under microwave (MW) radiation in a Milestone Ethos Plus Microwave oven for 2 h at 125 °C, leading to the formation of hydrocalumite. These as-prepared samples were named CaAl_{1-m}Fe_m, where *m* represents the amount of Fe³⁺ incorporated into the hydrocalumite-type solid, as fraction of the trivalent positions. In order to evaluate the photocatalytic activity, samples CaAl, CaAl_{0.90}Fe_{0.10}, CaAl_{0.80}Fe_{0.20} and CaFe were calcined at 400 °C, this temperature was selected taking into account the results shown by the thermal analysis of the solids and those reported in previous studies for hydrocalumites and hydrotalcites, as at this calcination temperature this sort of solids exhibit the largest specific surface area values, while higher temperatures lead to crystallization of the individual and mixed oxides [27,56–58]. For the calcined samples, “–400” was added to the name of the samples, denoting the calcination temperature, in Celsius. Considering hydrocalumite as the parent solid, it was doped by substituting Al³⁺ with Fe³⁺, in order to investigate the extent of the isomorphous substitution, and how the increase in Fe content influenced the catalytic performance. Thus, samples with *m* = 0, 0.1, 0.2, and 1 were selected in order to evaluate their photocatalytic activity in the degradation of ibuprofen.

2.3. Characterization Techniques

A Siemens D-5000 equipment was used to record the powder X-ray diffraction (PXRD) patterns of the samples ($\lambda = 0.154$ nm Cu-K α radiation, fixed divergence, 5°–70° (2 θ), scanning rate 2° (2 θ)/min, steps of 0.05°, 1.5 s/step). The crystalline phases formed were identified by comparison with the JCPDS-International Centre for Diffraction Data (ICDD[®]) database [59].

The thermogravimetric (TG) curves were recorded in an SDT Q600 apparatus (TA Instruments, New Castle, DE, USA) at a heating rate of 10 °C/min up to 900 °C and under oxygen (Air Liquide, Madrid, Spain, 99.999%) flow (50 mL/min).

The infrared spectra, FT-IR, were recorded in a Perkin-Elmer Spectrum Two instrument with a nominal resolution of 4 cm^{–1} from 4000 to 400 cm^{–1}, using KBr (Merck, grade IR spectroscopy, Kenilworth, NJ, USA) pressed pellets and averaging 12 scans to improve the signal-to-noise ratio.

Element chemical analyses for several elements were carried out by Inductively Coupled Plasma Optical Emission Spectrometry (ICP-OES) in a Yobin Ivon Ultima II apparatus (Nucleus Research Platform, University of Salamanca, Salamanca, Spain).

N₂ adsorption–desorption isotherms were recorded at –196 °C using a Micromeritics Gemini VII 2390T. Prior to analysis, N₂ flowed through the sample (ca 0.1 g) at 110 °C for 2 h to remove weakly adsorbed species. Specific surface areas were calculated by the Brunauer–Emmet–Teller (BET) method and the average pore diameter by the Barrett–Joyner–Halenda (BJH) method [60].

Scanning electron microscopy (SEM) images were obtained using a JEOL IT500 Scanning Electron Microscope at the Nucleus Research Platform (University of Salamanca, Spain).

2.4. Photodegradation Studies

The study of the catalytic performance of the solids was carried out on an MPDS-Basic system from Pechl Ultraviolet, with a PhotoLAB Batch-L reactor and a TQ150-Z0 lamp (power 150 W), integrated into a photonCABINET. Its spectrum is continuous, with the main peaks at 366 nm (radiation flux, Φ 6.4 W) and 313 nm (4.3 W). For this purpose, 750 mL of a solution of ibuprofen sodium salt in distilled water of concentration 50 ppm was introduced. An amount of 0.75 g of photocatalyst was added and magnetically stirred in the dark for

35 min to ensure the adsorption–desorption equilibrium [51], then the UV lamp was turned on. For taking samples for analyses, the illumination was cut off and the suspension was allowed to decant in order to reduce the losses of catalyst as much as possible. The samples taken were filtered with a filter Macherey-Nagel CHROMAFIL Xtra PA-20/25 of 0.22 μm . The solutions were analyzed by an ultraviolet-visible spectrophotometer coupled to a computer with UV WINLAB 2.85 software, following the evolution of the absorption band of ibuprofen at 222 nm. The reproducibility of the experiments was tested by duplicating some experiments, the difference in the values obtained always being lower than 1%.

In order to determine the by-products generated during UV degradation, selected solutions were analyzed after several reaction times by mass spectrometry (MS). The equipment used was an Agilent 1100 HPLC mass spectrometer coupled to an ultraviolet detector and an Agilent Trap XCT mass spectrometer. These analyses were performed at the Servicio Central de Análisis Elemental, Cromatografía y Masas (Universidad de Salamanca, Salamanca, Spain).

3. Results

3.1. Extraction of Aluminum

The aluminum content in the final extraction solution was 13,937 mg/L, while other elements were not found. The extraction and synthesis conditions described in our previous work [8,9] allowed us to obtain a pure aluminum solution, which was successfully used for the synthesis of the doped hydrocalumite solids.

3.2. Characterization of the Solids

3.2.1. Hydrocalumite Type Solids

Figure 1A shows the diffractograms of the synthesized solids. All the diffractograms showed the characteristic peaks of the hydrocalumite-type layered structure (ICDD card 01–072–4773). In an octahedral environment, the Fe^{3+} cation has an ionic radius of 55 pm while Al^{3+} has a radius of 54 pm [61], the similarity in size between the two cations allowed their isomorphic substitution in a similar system without important structural changes, although as the amount of Fe increased, the crystallinity of the final solid decreased [18], in spite of the fact that all the samples were submitted to a microwave aging process at 125 °C for 2 h. One of the peculiarities of hydrocalumite is its high degree of crystallinity compared to other LDHs; this is due to the fact that the Ca and Al octahedra are not randomly distributed in the sheets but are perfectly ordered due to the larger radius of Ca^{2+} compared to Mg^{2+} [8,30,62–65]. On the other hand, the similarity of radii between the divalent cation and the trivalent cation produces an increase in the disorder of the octahedra in the sheets [62,65]. In hydrocalumite, the large size difference between Ca^{2+} (100 pm) and Al^{3+} (54 pm) [8,61] contributes to an increase in the degree of ordering of the octahedra in the sheets [8,62,65]. As mentioned above, the radius of Fe^{3+} is slightly larger than the radius of Al^{3+} . When Al^{3+} is isomorphically substituted by Fe^{3+} , the $\text{Ca}^{2+}/\text{M}^{3+}$ radius ratio decreases, which implies an increase in the degree of disorder of the octahedra in the sheets with respect to hydrocalumite. Other phases were not detected by PXRD.

As described above, LDHs consist of $[\text{M}(\text{II})_{1-x}\text{M}(\text{III})_x(\text{OH})_2]^{x+}$ octahedral sheets. In the case of hydrocalumite, M(II) is Ca^{2+} and M(III) is Al^{3+} , the main difference between hydrocalumite with other LDHs is that the Ca and Al octahedra are not randomly arranged but are ordered [30,63]. This higher order implies more intense and narrower diffraction peaks than in other LDH, and peaks due to diffraction by planes (003), (006), (110) and (009) are present in the diffractograms of both hydrocalumite and other LDHs [64,65]. As shown in Figure 1A, the samples showed a clear preferred orientation, which coincided with the direction of sheet stacking (crystallographic direction c), in agreement with the high intensity of the (003) and (006) peaks. The main difference between the CaAl and CaFe samples was observed in the (110) plane peak, this diffraction peak shifted to lower diffraction angles when all Al^{3+} were replaced by Fe^{3+} ($m = 1$) (Figure 1B,C). The interlayer spacing from the (110) diffraction peak allowed us to calculate the value of the lattice

parameter a ($a = 2d_{(110)}$) and from the (003) and (006) spacing values the parameter c was calculated ($c = 3/2[d_{(003)} + 2d_{(006)}]$) [62]. These cell parameters were calculated for all the synthesized solids (Table 1); the literature reported that the a and c parameters for hydrocalumite are 0.575 nm and 2.349 nm, respectively (ICDD 01-072-4773), while for $\text{Ca}_2\text{Fe}(\text{OH})_6\text{Cl}\cdot 2\text{H}_2\text{O}$ these parameters are $a = 0.587$ nm and $c = 2.336$ nm [65]. Cell parameters of a varied between 0.574 and 0.586 nm in the prepared solids, all values of a were found to be within the range of theoretical values reported in the literature. Although the size difference between Fe^{3+} and Al^{3+} is very small, ionic radii 55 pm and 54 pm, respectively, it affected the a parameter, which was larger when the trivalent cation was entirely Fe^{3+} than when the trivalent cation was Al^{3+} . Figure 2 shows the variation of the a parameter with composition, as the amount of Fe^{3+} in the structure increased, the parameter a also increased, according to Vegard's Law. Thus, the amount of incorporated Fe^{3+} could be estimated from the lattice parameter a determined by PXRD by the expression $y = 0.0012x + 5.742$, where y represents the lattice parameter a and x represents the percentage of Fe^{3+} as a trivalent cation. On the other hand, lattice parameter c varied between 2.356 and 2.331 nm, very close to the expected value. However, a small decrease was observed as the Fe^{3+} content increased. The lattice parameters a and c showed an opposite trend. The parameter c depends on the charge, size and orientation of the interlayer anions [65,66]; in this case, the interlayer anion was chloride; therefore, these small variations found could be attributed to differences in the degree of hydration as shown in Table 1. Moreover, due to the basic character of these solids, it was possible that they fixed atmospheric CO_2 , incorporating traces of carbonate anion in the interlayer space, influencing on the value of this parameter. The values of parameter c were similar to those reported in the literature for $\text{Ca}_2\text{Al}(\text{OH})_6\text{Cl}\cdot 2\text{H}_2\text{O}$ ($c_{\text{theoretical}} = 2.349$ nm and $c_{\text{experimental}} = 2.356$ nm) and $\text{Ca}_2\text{Fe}(\text{OH})_6\text{Cl}\cdot 2\text{H}_2\text{O}$ ($c_{\text{theoretical}} = 2.336$ nm and $c_{\text{experimental}} = 2.331$ nm).

Table 1. Parameters determined for the synthesized solids.

Sample	a (nm) *	c (nm) **	Fe/M^{3+} (%) ***	$\text{Ca}^{2+}/\text{M}^{3+}$ Molar Ratio	$D_{(003)}$ (nm)	$D_{(001)}$ (nm)	S_{BET} (m^2/g)	Average Pore Diameter (nm)	Hydration Water (wt. %) ****
CaAl	0.574	2.356	0.00	2.05	37	82	12	8.7	12.3
CaAl _{0.95} Fe _{0.05}	0.575	2.354	5.91	1.96	33	66	15	9.2	12.9
CaAl _{0.90} Fe _{0.10}	0.576	2.354	8.87	1.83	38	45	13	6.2	12.1
CaAl _{0.80} Fe _{0.20}	0.576	2.355	19.77	1.83	32	60	20	8.2	15.7
CaAl _{0.60} Fe _{0.40}	0.577	2.350	38.71	1.90	35	21	22	8.9	11.9
CaAl _{0.40} Fe _{0.60}	0.579	2.346	60.68	1.54	34	21	28	9.0	11.7
CaAl _{0.20} Fe _{0.80}	0.582	2.341	82.65	1.26	33	26	32	8.2	11.5
CaFe	0.586	2.331	100	1.68	37	75	27	9.3	11.1

* a theoretical hydrocalumite = 0.575 nm and a_{CaFe} theoretical = 0.587 nm [65]. ** c theoretical hydrocalumite = 2.349 nm and c_{CaFe} = 2.336 nm [65]. *** Percentage of Fe^{3+} occupying trivalent positions. **** End of the first mass loss (~200 °C).

The crystallite sizes of the synthesized solids along the packing directions (003) ($d_{(003)}$) and (110) ($d_{(110)}$) are also shown in Table 1. The crystal size (D) was calculated from Scherrer's equation ($D = \frac{k\lambda}{\beta \cos \theta}$; $k = 0.94$; $\lambda = 0.154$ nm; $\theta =$ Bragg diffraction angle; $\beta = \sqrt{B^2 - b^2}$; $B = \text{FWHM}_{(hkl)}$ (rad); $b =$ instrument width (rad)) [67]. The crystal size along the sheet stacking direction ($d_{(003)}$) remained practically constant, showing values between 32 and 38 nm. However, in the (110) direction there was a decrease in the crystal size as the amount of Fe^{3+} in the structure increased, except for the CaFe sample, whose value approached that of the CaAl sample again.

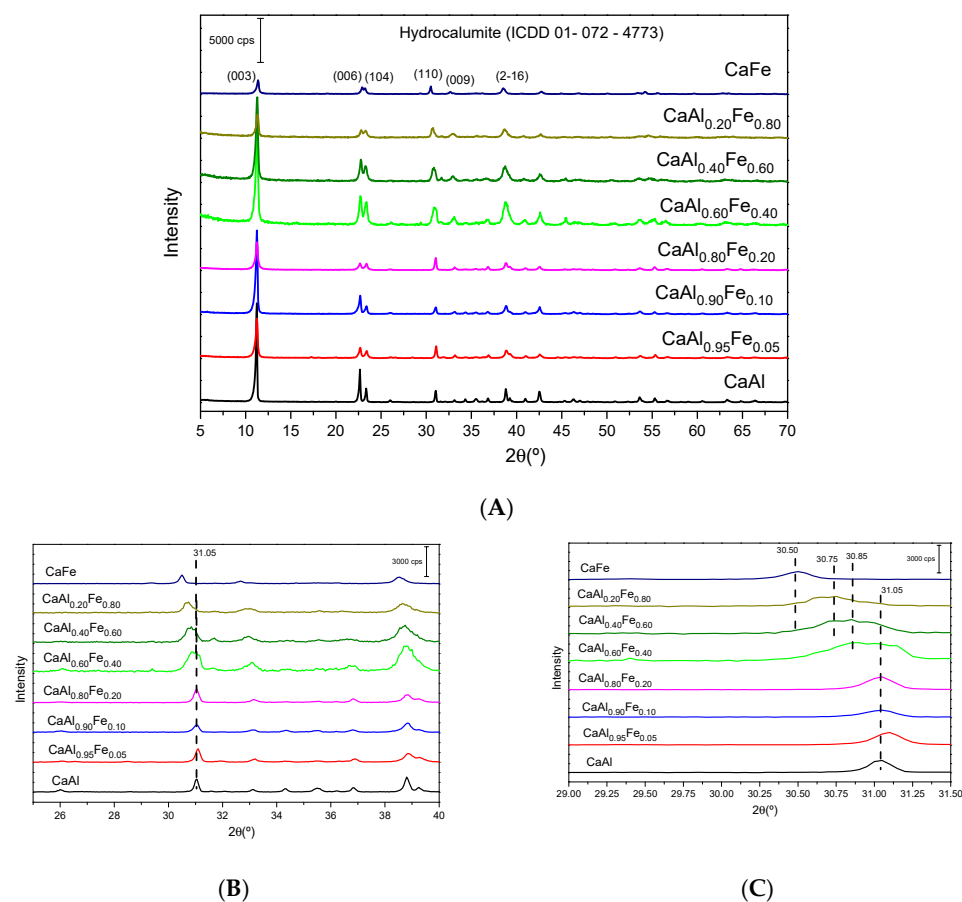


Figure 1. X-ray patterns of samples synthesized: (A) shows X-ray patterns of all samples, while (B,C) show in detail the variation in the position of the peak due to the (110) plane diffraction with the increasing of the Fe³⁺ content in the solids.

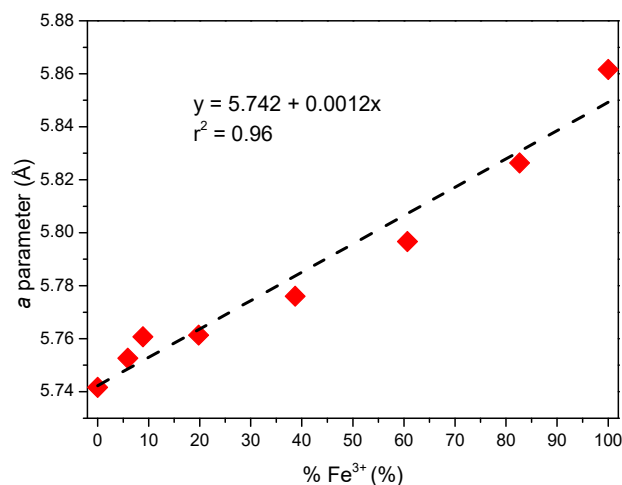


Figure 2. Variation of parameter *a* with the amount of Fe³⁺ incorporated. Red points = experimental values; Dashed line: straight adjustment.

Table 1 also shows the amount of Fe³⁺ present in the solids. All amounts agreed with the theoretical amount of Fe³⁺ predicted from the composition of the original solutions. Regarding the Ca²⁺/M³⁺ molar ratio, it moved away from the theoretical value of 2 for Ca/Al hydrocalumite as the Fe³⁺ content increased.

Figure 3 shows the FT-IR spectra of the samples. There were few differences between all the solids. All of them showed bands between 3600 and 3400 cm⁻¹ that corresponded

to the stretching vibration of the O–H bonds. The band at 3632 cm^{-1} was assigned to the stretching vibration of the AlO–H bonds, while the band due to the stretching vibration of the CaO–H bonds was located at 3471 cm^{-1} . On the other hand, as the Fe^{3+} content increased in the samples, a band appeared at 3591 cm^{-1} , which could be assigned to the stretching vibration of the FeO–H bonds [54,57]. In this zone, the bands corresponding to the hydroxyl groups of the water molecules located in the interlayer space were also found [54,68,69]. The band at 1615 cm^{-1} was due to the bending vibration of water, which confirmed its presence in the interlayer space. The presence of CO_3^{2-} ion was confirmed by the band at 1414 cm^{-1} . During the synthesis of the solids, special care was taken to work in an inert atmosphere and decarbonated water was used to avoid the formation of calcite, however, it was possible that the samples fixed atmospheric CO_2 during their handling, producing the incorporation of traces of carbonate. The band located at 1414 cm^{-1} increased its intensity as the Fe^{3+} content increased, in such a way that for the CaAl sample this band was practically not observed. The presence of CO_3^{2-} in the interlayer space was confirmed by the existence of bands at 1506 cm^{-1} and 870 cm^{-1} in the samples with higher Fe^{3+} content (CaFe, $\text{CaAl}_{0.20}\text{Fe}_{0.80}$ and $\text{CaAl}_{0.40}\text{Fe}_{0.60}$) [31,70]. This seemed to contradict the PRXD results, since the larger the size of the interlayer anion, the higher the value of the reticular parameter c should be. The diameter of CO_3^{2-} is 378 pm [61], while that of Cl^- is 336 pm [61]; according to these values, the samples that present a band at 1414 cm^{-1} should present a higher value of the reticular parameter c . However, according to the values in Table 1, no increase in parameter c was observed with the presence of carbonate in the samples, so the differences in parameter c observed can be attributed to small variations in the degree of hydration of the anions located in the interlayer space. The carbonate may then be adsorbed on the surface or even in the form of very small particles not detectable by powder X-ray diffraction. The bands at 797 cm^{-1} , 739 cm^{-1} , 575 cm^{-1} and 421 cm^{-1} were assigned to M–O bonds, where M is Ca^{2+} , Al^{3+} or Fe^{3+} [54,68,69,71].

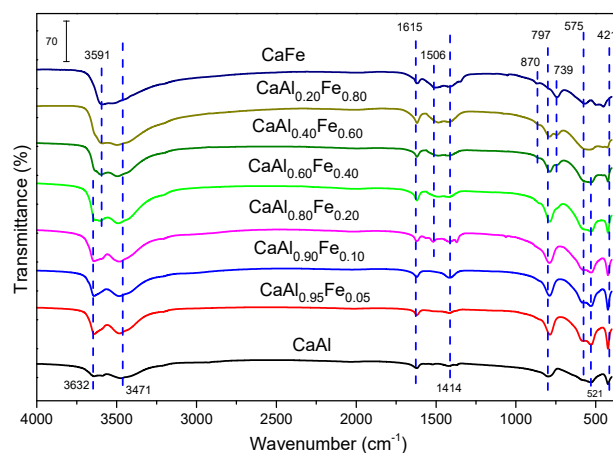


Figure 3. FT—IR spectra of the samples.

The TG and DTG curves of the samples are shown in Figure 4, all of them were very similar to each other, showing thermal decomposition processes characteristic of LDH [26,66,72], as in all cases the phases identified by PXRD corresponded to LDH and other phases were not detected. In all cases, three main mass loss steps were observed, with a total mass loss between 28 and 36% (theoretical total mass loss for complete dehydration/dehydroxylation of $\text{Ca}_2\text{Al}(\text{OH})_6\text{Cl}\cdot 2\text{H}_2\text{O}$ would be 32.1% and for $\text{Ca}_2\text{Fe}(\text{OH})_6\text{Cl}\cdot 2\text{H}_2\text{O}$ it would be 29.1%). The first one was located at a temperature between $140\text{--}150\text{ }^\circ\text{C}$, corresponding to the loss of hydration water located in the interlayer space or chemically bound to LDH [26,66,72]. The second mass loss appeared close to $300\text{ }^\circ\text{C}$ and corresponded to the dehydroxylation of the layers. As the Fe^{3+} content increased, the temperature at which the process took place decreased, from $328\text{ }^\circ\text{C}$ for the CaAl sample to $270\text{ }^\circ\text{C}$ for the CaFe sample, which indicated that the Fe–OH bonds were weaker than the Al–OH

bonds, which was in agreement with the FT-IR results. The third and last mass loss was located close to 700 °C and could be associated with the decarbonization of the samples. However, in our previous work, this last stage was shown to be compatible with the elimination of a water molecule, thus completing the dehydroxylation process to form the corresponding oxychloride [57]. In addition, in some samples (CaAl_{0.80}Fe_{0.20} or CaFe) an additional mass loss was observed at a temperature below 100 °C, due to the elimination of physisorbed water [63,73]. Considering this thermal behavior, 400 °C was considered the ideal temperature for the calcination of the solids.

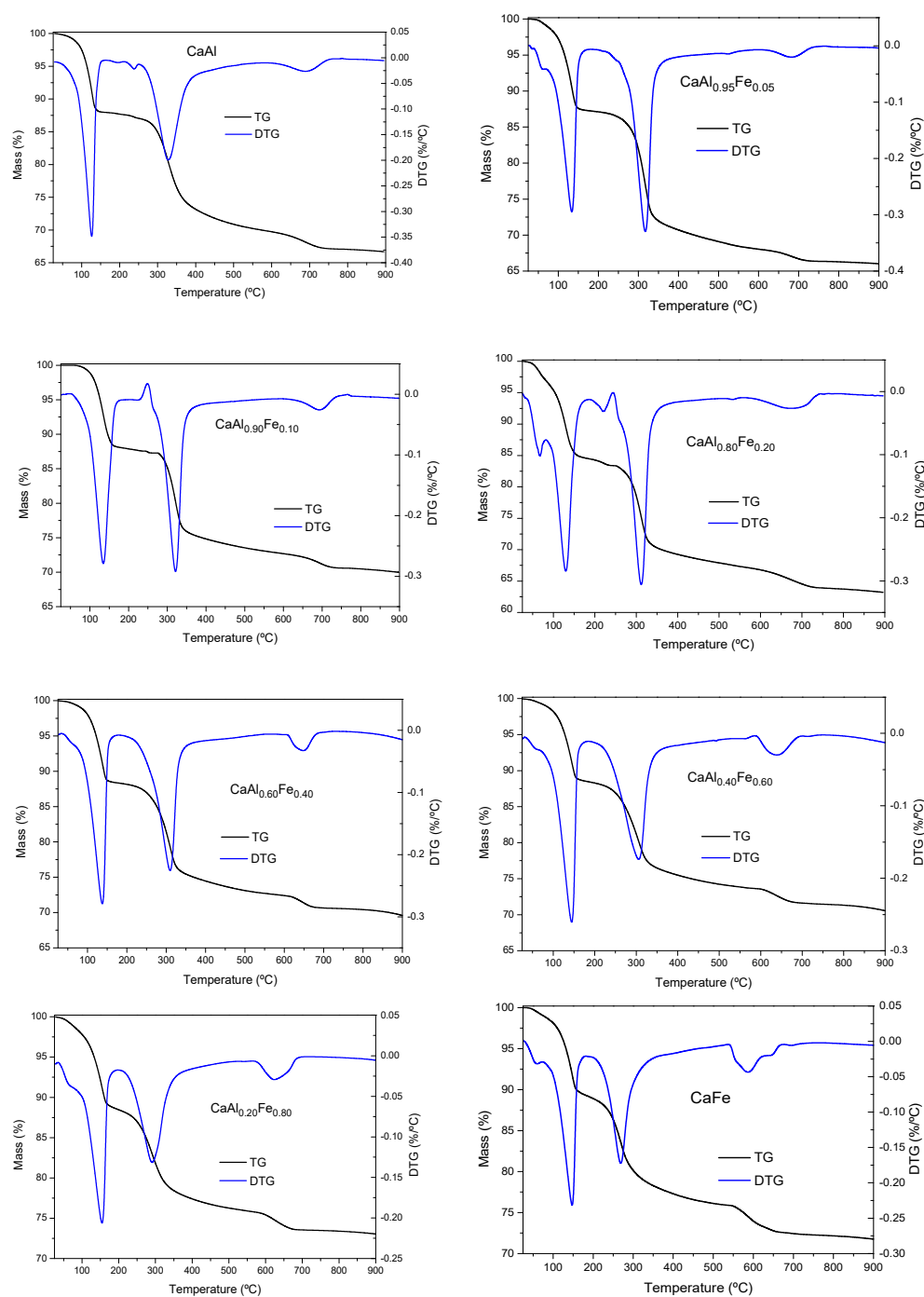


Figure 4. TG and DTG curves of the solids synthesized.

According to the IUPAC isotherm classification criteria [60], all synthesized solids showed type II N₂ adsorption isotherms (Figure 5). In addition, some of them showed a

small hysteresis loop of type H3 after recording the desorption branch, which corresponded to the presence of plate-like particle aggregates leading to slit-like pores [60]. All samples presented low values of BET-specific surface area (Table 1), with a maximum of $32 \text{ m}^2/\text{g}$ for sample $\text{CaAl}_{0.20}\text{Fe}_{0.80}$ and with an average pore width in the mesopore range. In general, as the amount of Fe^{3+} in the solid increased, there was an increase in S_{BET} values, although, for values $m \geq 0.60$, the increase in Fe^{3+} content did not cause an increase in S_{BET} , with $\text{CaAl}_{0.40}\text{Fe}_{0.60}$, $\text{CaAl}_{0.20}\text{Fe}_{0.80}$ and CaFe showing similar S_{BET} values (all of them higher than those of the samples with lower Fe^{3+} content). This was in agreement with PXRD data because as the Fe^{3+} content increased, the crystallinity of the samples decreased.

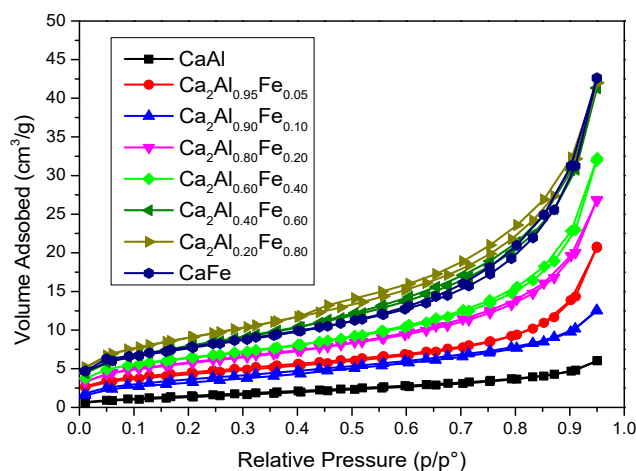


Figure 5. Nitrogen adsorption–desorption isotherms of the samples.

3.2.2. Solids Calcined at 400°C

Figure 6 shows the diffractograms of the samples calcined at 400°C . With respect to the LDH-type solids before calcination, the layered structure completely disappeared, giving rise to the formation of amorphous mixed oxides. In the CaFe-400 sample, the appearance of diffraction peaks corresponding to magnetite (Fe_3O_4 , ICDD card 01–072–6170) and hematite (Fe_2O_3 , ICDD card 01–084–0311) phases was observed. In the samples with lower Fe^{3+} or no Fe^{3+} content at all, no crystalline phases were observed.

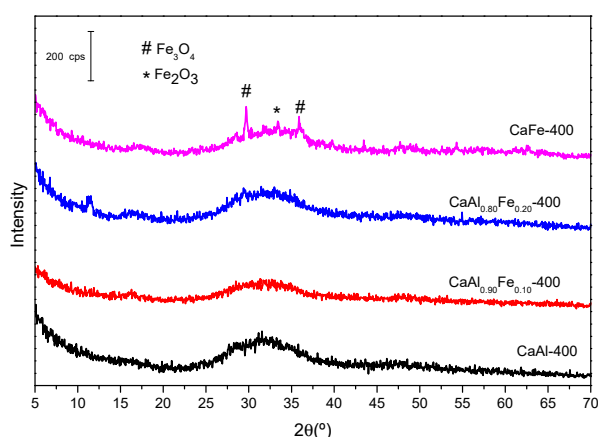


Figure 6. X-ray patterns of samples calcined at 400°C .

The FT-IR spectra of the samples calcined at 400°C are shown in Figure 7. In the samples with low Fe^{3+} content (CaAl-400 , $\text{CaAl}_{0.90}\text{Fe}_{0.10}$ and $\text{CaAl}_{0.80}\text{Fe}_{0.20}$) a broad band centered at 3565 cm^{-1} was observed, due to the stretching vibrational mode of the hydroxyl groups. This band was broad and presented a shoulder centered at 3428 cm^{-1} , being composed of the superposition of hydroxyl group bands coming from several

environments [58]. The presence of water was confirmed by its bending band at 1624 cm^{-1} . On the other hand, the characteristic bands of carbonate appeared again at 1419 cm^{-1} , 1496 cm^{-1} and 879 cm^{-1} [31,58,70]. This carbonate species may be formed during the precipitation of the starting solid or adsorbed due to the basic character of the hydrocalumites, in both cases by fixation of atmospheric CO_2 . Finally, the band located at 596 cm^{-1} as well as others located in the region between 800 cm^{-1} and 400 cm^{-1} (not labeled in Figure 7) can be attributed to M–OH bonds, where M can be Ca^{2+} , Al^{3+} or Fe^{3+} [58]. The band at 814 cm^{-1} showed a shoulder on its left-hand side which could be attributed to the presence of carbonate in the samples, and it can overlap with the band at 870 cm^{-1} with characteristics of the carbonate ion. However, this band was not present in the spectrum of the CaFe-400 sample, suggesting that it can be attributed to the Al–OH bond, but band assignment in this region is complicated due to band overlapping and broadness of the bands.

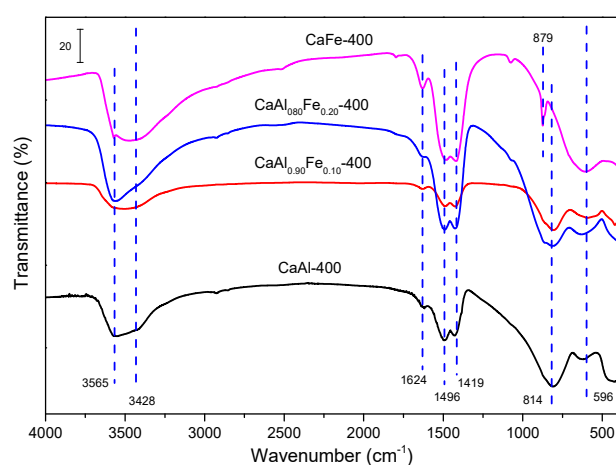


Figure 7. FT-IR spectra of the samples calcined at $400\text{ }^{\circ}\text{C}$.

Figure 8 shows the nitrogen adsorption–desorption isotherms of the solids calcined at $400\text{ }^{\circ}\text{C}$. All isotherms are type II, according to the IUPAC classification criteria [60]. Only the CaFe-400 sample showed a type H3 hysteresis loop [60]. Although the calcination should remove part of the interlayer water, the calcination process did not produce an increase in S_{BET} in the samples (Table 2), but a remarkable decrease, mainly associated with the loss of the layered structure (vide infra). Thus, for example, for the café sample, the S_{BET} decreased from $27\text{ m}^2/\text{g}$ to $16\text{ m}^2/\text{g}$ under calcination, probably by the loss of the layered structure and the formation under calcination of crystallites that may block access to the porosity. On the other hand, the average pore width remained in the mesopore range.

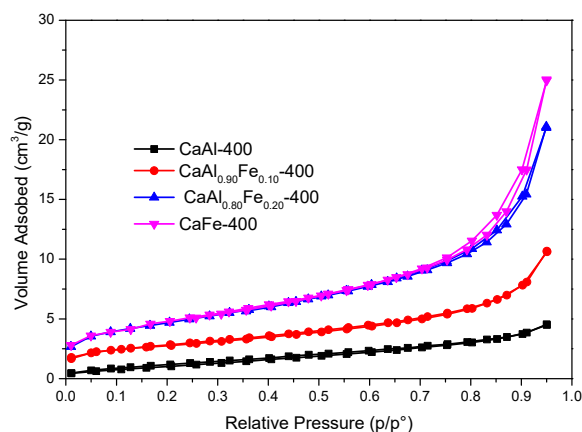
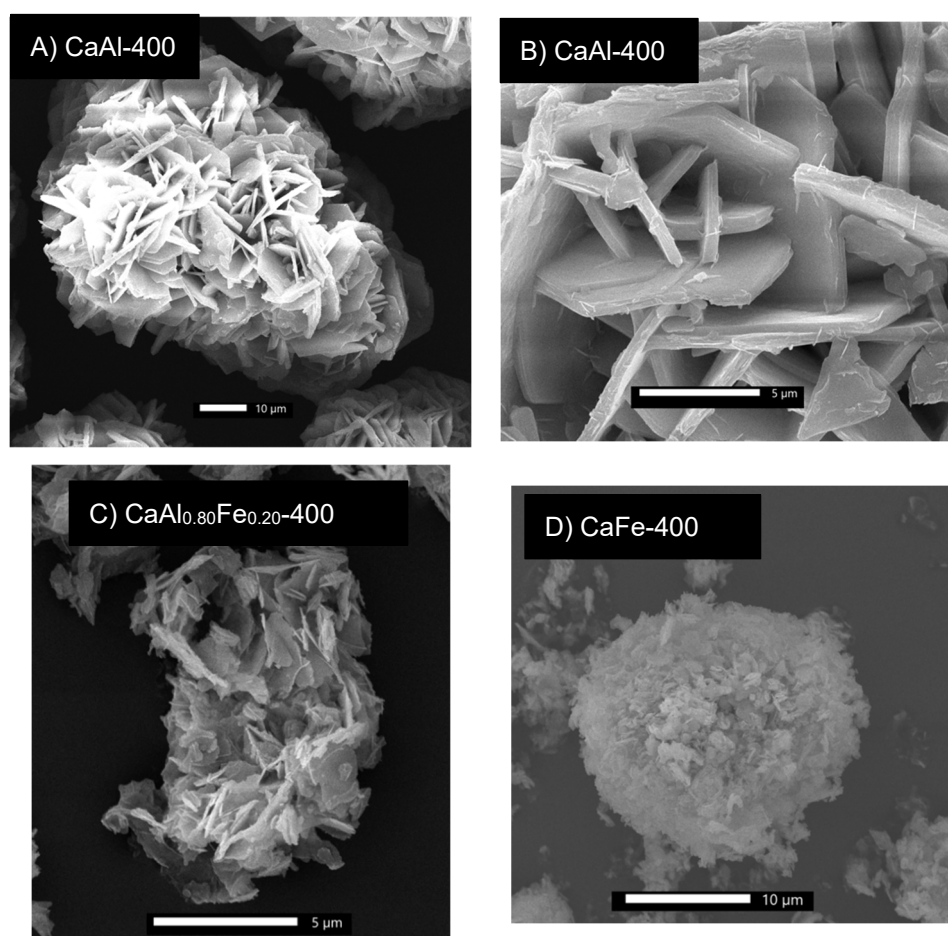


Figure 8. Nitrogen adsorption–desorption isotherms of samples calcined at $400\text{ }^{\circ}\text{C}$.

Table 2. S_{BET} and average pore diameter of samples calcined at 400 °C.

Sample	S_{BET} (m^2/g)	Average Pore Diameter (nm)
CaAl-400	5	5.5
CaAl _{0.90} Fe _{0.10} -400	10	7.3
CaAl _{0.80} Fe _{0.20} -400	16	9.9
CaFe-400	16	10.1

Figure 9A,B show micrographs of the CaAl-400 sample. Aggregates of particles of size 70–80 μm are observed, consisting of hexagonal plate-shaped particles characteristic of LDH-type compounds [8]. However, unlike the uncalcined LDHs, the plate-shaped particles were aggregated into larger particles, showing that the layered structure was maintained at this calcination temperature [18,32,74]. However, sintering of the hexagonal plate-shaped particles with each other was observed. On the other hand, Figure 9C shows an SEM micrograph of the CaAl_{0.80}Fe_{0.20}-400 sample. Aggregates of the hexagonal plate-shaped particles were observed, although of considerably smaller size (5–10 μm) than in the case of the CaAl-400 sample and with an appearance of greater sponginess. Finally, Figure 9D,E show two SEM micrographs of the CaFe-400 sample. In this case, aggregates of particles with a spongy appearance were observed, totally different from those observed in the CaAl sample. This spongy aspect could justify the higher S_{BET} value for this solid. In the SEM micrograph of higher magnification (Figure 9E), particles in the form of a hexagonal plate remained, however, a higher degree of sintering for the CaAl-400 sample was observed.

**Figure 9.** *Cont.*

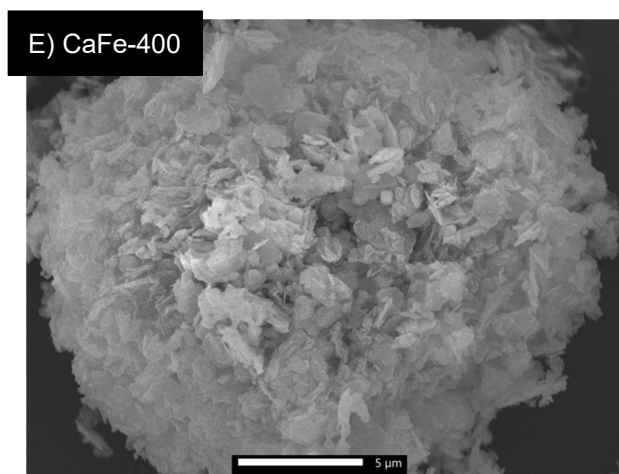


Figure 9. SEM micrographs of samples calcined at 400 °C. (A,B) show micrographs of CaAl-400 sample. (C) belongs to $\text{CaAl}_{0.80}\text{Fe}_{0.20}$ -400 sample and (D,E) show SEM micrographs of CaFe-400 sample.

3.3. Photocatalytic Application

Figure 10 shows the photodegradation of ibuprofen by the action of ultraviolet light in the absence and presence of LDHs calcined at 400 °C. Initially, the photodegradation of ibuprofen was evaluated in the absence of catalyst (photolysis) observing that 78% of the initial ibuprofen still remained after 152 min of irradiation with ultraviolet light in the photoreactor, i.e., in the presence of ultraviolet light but without photocatalyst, 22% of the initial ibuprofen was degraded, higher than the value reported in the literature [38]. When calcined LDH was added, the removal of the contaminant by adsorption was evaluated. For this purpose, the aqueous solution containing 50 ppm ibuprofen and 0.75 g of the photocatalyst was kept under stirring in the dark, and samples were taken at 0, 5, 10, 15, 20 and 35 min, finding that there was no elimination of ibuprofen by adsorption during this time. Subsequently, the ultraviolet light lamp was turned on and new aliquots were taken at various times. The concentration of the contaminant rapidly dropped to ca. 24% of the initial concentration after 42 min switching on the lamp (T_{77} , total time 77 min, 42 from the beginning of photocatalysis) with all the photocatalysts used. Up to this point, no major differences were observed in the percentage of ibuprofen degraded depending on the photocatalyst used; however, after this time of contact, the photocatalyst did not contain Fe^{3+} (CaAl-400) showed higher degradation percentages. Thus, 152 min after the lamp was switched on, the percentage of the initial ibuprofen remaining in the solution was only 4.7% for the CaAl sample and between 13% and 17% for the rest of the samples, those containing Fe^{3+} . Thus, for long times CaAl-400 photocatalyst showed the best performance and the presence of Fe^{3+} caused a low negative effect, this may be due to the formation of oxides or mixed oxides of Ca^{2+} , Fe^{3+} and Al^{3+} which did not possess photocatalytic properties, even though some of the properties of the photocatalysts were improved, such as S_{BET} which increased with increasing the Fe^{3+} content. This behavior is similar to that reported on LDH-ZnFe systems, also calcined at 400 °C [51], in which ibuprofen degradation improved as the Zn/Fe ratio increased.

As indicated above, the photocatalyst obtained by calcination of LDHs at 400 °C that showed the best performance was CaAl-400; Figure 11A shows the ultraviolet-visible spectra of the aliquots taken at different times when this catalyst was used. During the “adsorption experiment”, before the lamp was switched on (35 min) there was no variation in the characteristic band of ibuprofen at 222 nm [38,75], while after switching on the UV lamp the intensity of this band decreased, denoting photodegradation. Moreover, already for times T_{42} and T_{48} (7 min and 13 min after turning on the UV light, respectively), a new band appeared at 259 nm. This band may be due to the formation of a by-product of the degradation of ibuprofen; this band disappeared at longer times, indicating that this temporary intermediate was also photodegraded. For the rest of the photocatalysts, and

also in the photolysis experiment, the evolution of the spectra was similar to that shown for the CaAl-400 sample.

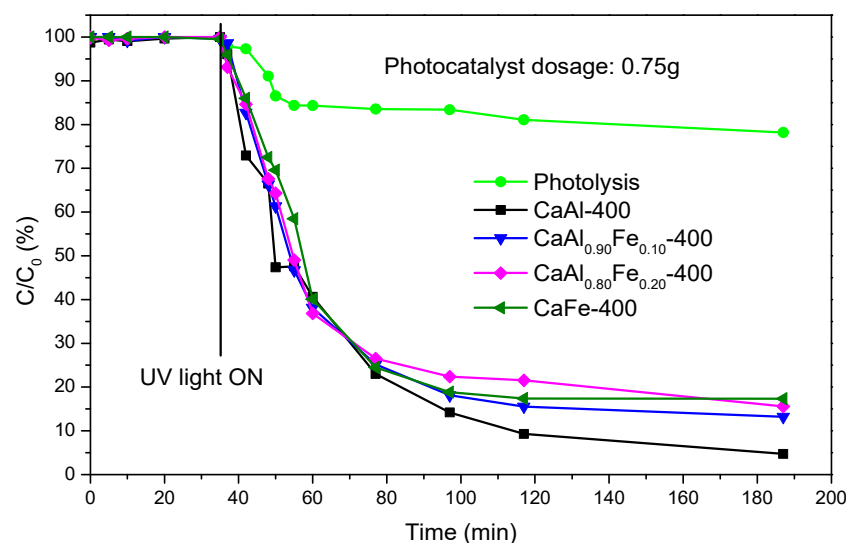


Figure 10. Ibuprofen degradation using samples calcined at 400 °C (photolysis is included for comparison).

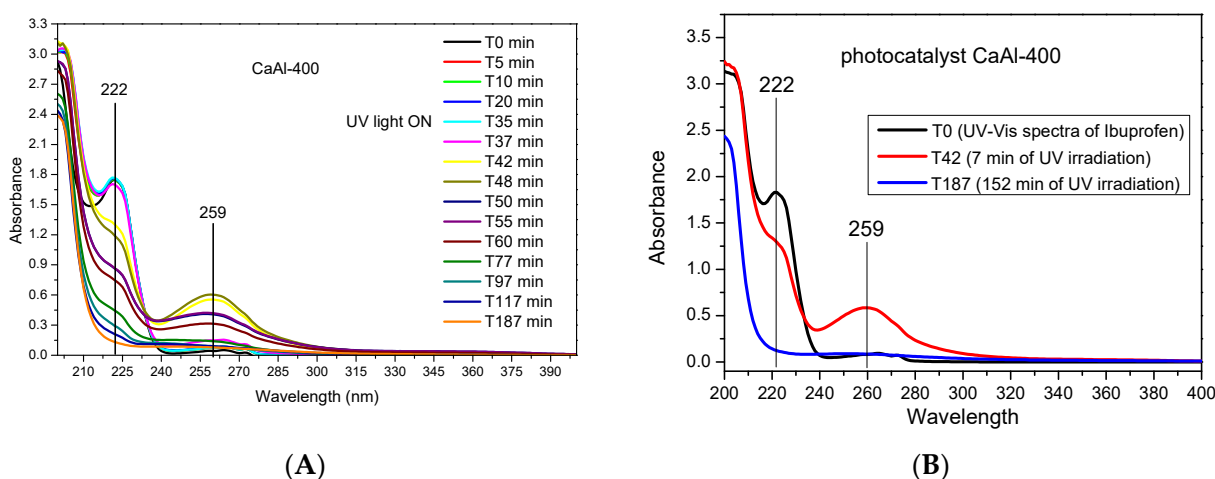


Figure 11. Ultraviolet-visible spectra of samples taken at different times when the CaAl-400 photocatalyst was used. (A) UV-Vis spectra of all samples taken at different times; (B) UV-Vis spectra of ibuprofen (T_0), aliquot at T_{42} and aliquot at T_{187} .

According to the most recent literature [40,44], the main photodegradation metabolites generated in the removal of ibuprofen by chemical methods (AOPs) were: 4-isobutylphenol ($C_{10}H_{14}O$), hydratropic acid ($C_9H_{10}O_2$), 4-(1-carboxyethyl)benzoic acid ($C_{10}H_{10}O_4$), 4-ethylbenzaldehyde ($C_9H_{10}O$), 2-[4-[4-(1-hydroxy-2-methylpropyl)phenyl]propanoic acid ($C_{13}H_{18}O_3$), 1-(4-isobutylphenyl)-1-ethanol ($C_{12}H_{18}O$), 4-acetylbenzoic acid ($C_9H_8O_3$), 1-isobutyl-4-vinylbenzene ($C_{12}H_{16}$) and 4-isobutylacetophenon ($C_{12}H_{16}O$). However, none of these metabolites were identified in the present work. As indicated, the spectrum of ibuprofen only showed the absorption maximum located at 222 nm (Figure 11B), but already for the aliquot taken 7 min after starting irradiation (T_{42}) an absorbance maximum at 259 nm was observed, and at the same time the HPLC-MS analysis showed the presence of two compounds: $C_{13}H_{18}O_2$ (ibuprofen) and a compound with formula $C_{13}H_{18}O_4$. This compound may correspond to a hydroxylated derivative of ibuprofen formed by a mechanism involving $\bullet OH$ radicals. In fact, the literature has listed various hydroxylated by-products in the photocatalytic degradation of ibuprofen [38,40,44,76,77], but the forma-

tion of one or another by-product is not clear and depends on the photocatalyst used. The band at 259 nm decreased as the irradiation time with UV light increased (Figure 11), so that for an irradiation time of 152 min this band practically did not exist and neither did the ibuprofen band, suggesting the disappearance of the aromatic ring. The aliquot of sample T₁₈₇ was also analyzed by HPLC–MS, again finding a compound of formula C₁₃H₁₈O₄ and, although its concentration could not be quantified, both UV–Vis and HPLC–MS indicated a clear decrease in its presence from T₄₂ to T₁₈₇ aliquot. However, this did not mean that ibuprofen was completely and safely mineralized, as non-aromatic by-products may still remain in the solution. In this regard, further studies are required in order to better understand the performance of hydrocalumite-type solids and the reaction mechanism, also analyzing the mineralization of the pollutant by analysis of the total organic carbon.

4. Conclusions

Hydrocalumite LDH of formula Ca₂Al_{1–m}Fe_m(OH)₆Cl·2H₂O were synthesized by the coprecipitation method, using as a source of aluminum one of the most hazardous wastes generated during aluminum recycling. The slags were treated in a basic medium under reflux conditions and the extraction solution was used as an aluminum source. The solids synthesized by the coprecipitation method were submitted to a microwave treatment at 125 °C for 2 h. In all cases, the corresponding LDH was obtained, the crystallinity decreasing as the Fe³⁺ content in the final solid increased, and the 110 diffraction peak shifted towards the lower two values. The lattice parameter *a*, determined from the (110) diffraction peak spacing, correlated with the amount of Fe³⁺ incorporated into the LDH, obeying Vegard's law. In spite of working in an inert atmosphere and using decarbonated water, the FT–IR results showed the presence of carbonate in the solids, due to the fixation of atmospheric CO₂ by the samples, due to their high basic character. As the amount of Fe³⁺ in the solids increased, the S_{BET} increased and the degree of hydration of the LDH decreased.

When LDH was calcined at 400 °C, a mixture of non-crystalline oxides was obtained, without crystalline phases, except in the CaFe-400 sample, where small diffraction peaks corresponding to hematite and magnetite were observed. The FT–IR results showed the presence of carbonate ions, possibly coming from the fixation of atmospheric CO₂, as well as the permanence of physisorbed water. The S_{BET} of the solids calcined at 400 °C was hardly modified for the samples with null or low Fe³⁺ content. However, for the CaFe-400 sample, a decrease in S_{BET} was observed.

The photocatalytic performance of the calcined solids was evaluated in the removal of ibuprofen. All the catalysts employed facilitated the degradation of this pollutant. However, as the Fe³⁺ content in the solid increased, the catalytic performance decreased. The catalyst that showed the best results was CaAl-400. In the same way, the HPLC–Mass and UV–Vis analyses of the aliquots taken at different times showed only the presence of a di-hydroxylated derivative, besides ibuprofen. This by-product reached its maximum formation after 7 min of irradiation, subsequently, it also degraded, although was still present in the solution after 152 min of irradiation with UV light. No other characteristic by-products of ibuprofen degradation were identified. More studies are required in order to investigate the effect of other parameters such as catalyst dosage, pH, etc., and mainly to elucidate the performance of hydrocalumite-type solids and the photodegradation mechanism.

Author Contributions: A.J.: Data curation, Formal analysis, Investigation, Methodology, Validation, Writing—original draft, Writing—review. M.V.: Data curation, Formal analysis, Investigation, Methodology, Validation. A.M.: Data curation, Formal analysis, Investigation, Methodology, Validation, Writing—original draft. R.T.: Conceptualization, Data curation, Formal analysis, Methodology, Supervision, Validation, Writing—review and editing. A.G.: Conceptualization, Data curation, Formal analysis, Methodology, Validation, Writing—review and editing. M.A.V.: Conceptualization, Data curation, Formal analysis, Methodology, Project administration, Resources, Supervision, Validation, Writing—review and editing. All authors have read and agreed to the published version of the manuscript.

Funding: This research was funded by Universidad de Salamanca (Plan I-B2).

Acknowledgments: This work belongs to the End-of-Degree work of Marta Valverde, supervised by Miguel Angel Vicente and Alejandro Jiménez, and is a section of the Ph. D. Thesis of Alejandro Jiménez, supervised by Miguel Angel Vicente and Vicente Rives. This article is included in the ChemEngineering Special Issue dedicated to Vicente Rives on his retirement (A Themed Issue in Honor of Vicente Rives, https://www.mdpi.com/journal/ChemEngineering/special_issues/honor_Vicente). With our participation in this Special Issue we want to express our immense gratitude to Vicente Rives for his help—as a teacher, as a researcher and as a friend—during all these years. A.J. thanks the Universidad de Salamanca and Banco Santander for a predoctoral contract.

Conflicts of Interest: The authors declare no conflict of interest.

References

1. World Bureau of Metal Statistics. Available online: <http://www.world-bureau.com/> (accessed on 1 June 2022).
2. Gil, A. Management of the Salt Cake from Secondary Aluminum Fusion Processes. *Ind. Eng. Chem. Res.* **2005**, *44*, 8852–8857. [[CrossRef](#)]
3. He, L.; Shi, L.; Huang, Q.; Hayat, W.; Shang, Z.; Ma, T.; Wang, M.; Yao, W.; Huang, H.; Chen, R. Extraction of Alumina from Aluminum Dross by a Non-Hazardous Alkaline Sintering Process: Dissolution Kinetics of Alumina and Silica from Calcined Materials. *Sci. Total Environ.* **2021**, *777*, 146123. [[CrossRef](#)] [[PubMed](#)]
4. Tsakiridis, P.E. Aluminium Salt Slag Characterization and Utilization—A Review. *J. Hazard. Mater.* **2012**, *217–218*, 1–10. [[CrossRef](#)]
5. Tsakiridis, P.E.; Oustadakis, P.; Moustakas, K.; Agatzini, S.L. Cyclones and Fabric Filters Dusts from Secondary Aluminium Flue Gases: A Characterization and Leaching Study. *Int. J. Environ. Sci. Technol.* **2016**, *13*, 1793–1802. [[CrossRef](#)]
6. Mahinroosta, M.; Allahverdi, A. Hazardous Aluminum Dross Characterization and Recycling Strategies: A Critical Review. *J. Environ. Manag.* **2018**, *223*, 452–468. [[CrossRef](#)] [[PubMed](#)]
7. Jiménez, A.; Misol, A.; Morato, Á.; Rives, V.; Vicente, M.A.; Gil, A. Synthesis of Pollucite and Analcime Zeolites by Recovering Aluminum from a Saline Slag. *J. Clean. Prod.* **2021**, *297*, 126667. [[CrossRef](#)]
8. Jiménez, A.; Misol, A.; Morato, Á.; Rives, V.; Vicente, M.A.; Gil, A. Optimization of Hydrocalumite Preparation under Microwave Irradiation for Recovering Aluminium from a Saline Slag. *Appl. Clay Sci.* **2021**, *212*, 10217. [[CrossRef](#)]
9. Jiménez, A.; Rives, V.; Vicente, M.A.; Gil, A. A Comparative Study of Acid and Alkaline Aluminum Extraction Valorization Procedure for Aluminum Saline Slags. *J. Environ. Chem. Eng.* **2022**, *10*, 107546. [[CrossRef](#)]
10. Meshram, A.; Singh, K.K. Recovery of Valuable Products from Hazardous Aluminum Dross: A Review. *Resour. Conserv. Recycl.* **2018**, *130*, 95–108. [[CrossRef](#)]
11. EU Parliament. Directive 2010/75/EU of the European Parliament and of the Council of 24 November 2010 on Industrial Emissions (Integrated Pollution Prevention and Control). *Off. J. Eur. Union* **2010**, *334*, 17.
12. Gil, A.; Albeniz, S.; Korili, S.A. Valorization of the Saline Slags Generated during Secondary Aluminium Melting Processes as Adsorbents for the Removal of Heavy Metal Ions from Aqueous Solutions. *Chem. Eng. J.* **2014**, *251*, 43–50. [[CrossRef](#)]
13. Gil, A.; Korili, S.A. Management and Valorization of Aluminum Saline Slags: Current Status and Future Trends. *Chem. Eng. J.* **2016**, *289*, 74–84. [[CrossRef](#)]
14. Gil, A.; Arrieta, E.; Vicente, M.Á.; Korili, S.A. Application of Industrial Wastes from Chemically Treated Aluminum Saline Slags as Adsorbents. *ACS Omega* **2018**, *3*, 18275–18284. [[CrossRef](#)] [[PubMed](#)]
15. Das, B.R.; Dash, B.; Tripathy, B.C.; Bhattacharya, I.N.; Das, S.C. Production of η -Alumina from Waste Aluminium Dross. *Miner. Eng.* **2007**, *20*, 252–258. [[CrossRef](#)]
16. Yoldi, M.; Fuentes-Ordoñez, E.G.; Korili, S.A.; Gil, A. Zeolite Synthesis from Industrial Wastes. *Microporous Mesoporous Mater.* **2019**, *287*, 183–191. [[CrossRef](#)]
17. Gil, A.; Arrieta, E.; Vicente, M.A.; Korili, S.A. Synthesis and CO₂ Adsorption Properties of Hydrotalcite-like Compounds Prepared from Aluminum Saline Slag Wastes. *Chem. Eng. J.* **2018**, *334*, 1341–1350. [[CrossRef](#)]
18. Santamaría, L.; Vicente, M.A.; Korili, S.A.; Gil, A. Saline Slag Waste as an Aluminum Source for the Synthesis of Zn–Al–Fe–Ti Layered Double-Hydroxides as Catalysts for the Photodegradation of Emerging Contaminants. *J. Alloys Compd.* **2020**, *843*, 156007. [[CrossRef](#)]
19. Santamaría, L.; López-Aizpún, M.; García-Padial, M.; Vicente, M.A.; Korili, S.A.; Gil, A. Zn–Ti–Al Layered Double Hydroxides Synthesized from Aluminum Saline Slag Wastes as Efficient Drug Adsorbents. *Appl. Clay Sci.* **2020**, *187*, 105486. [[CrossRef](#)]
20. Santamaría, L.; García, L.O.; De Faria, E.H.; Ciuffi, K.J.; Vicente, M.A.; Korili, S.A.; Gil, A. M(II)-Al-Fe Layered Double Hydroxides Synthesized from Aluminum Saline Slag Wastes and Catalytic Performance on Cyclooctene Oxidation. *Miner. Eng.* **2022**, *180*, 107516. [[CrossRef](#)]
21. Rives, V. (Ed.) *Layered Double Hydroxides*; Nova Science Publishers, Inc.: New York, NY, USA, 2001.
22. Zhitova, E.S.; Pekov, I.V.; Chaikovskiy, I.I.; Chirkova, E.P.; Yapaskurt, V.O.; Bychkova, Y.V.; Belakovskiy, D.I.; Chukanov, N.V.; Zubkova, N.V.; Krivovichev, S.V.; et al. Dritsite, Li₂Al₄(OH)₁₂Cl₂·3H₂O, a New Gibbsite-Based Hydrotalcite Supergroup Mineral. *Minerals* **2019**, *9*, 492. [[CrossRef](#)]
23. Thiel, J.P.; Chiang, C.K.; Poepplmeier, K.R. Structure of lithium aluminum hydroxide dihydrate (LiAl₂(OH)₇·2H₂O). *Chem. Mater.* **1993**, *2*, 297–304. [[CrossRef](#)]

24. Takaki, Y.; Qiu, X.; Hirajima, T.; Sasaki, K. Removal Mechanism of Arsenate by Bimetallic and Trimetallic Hydrocalumites Depending on Arsenate Concentration. *Appl. Clay Sci.* **2016**, *134*, 26–33. [[CrossRef](#)]
25. Linares, C.F.; Moscoso, J.; Alzurutt, V.; Ocanto, F.; Bretto, P.; González, G. Carbonated Hydrocalumite Synthesized by the Microwave Method as a Possible Antacid. *Mater. Sci. Eng. C* **2016**, *61*, 875–878. [[CrossRef](#)] [[PubMed](#)]
26. Murayama, N.; Maekawa, I.; Ushiro, H.; Miyoshi, T.; Shibata, J.; Valix, M. Synthesis of Various Layered Double Hydroxides Using Aluminum Dross Generated in Aluminum Recycling Process. *Int. J. Miner. Process.* **2012**, *110–111*, 46–52. [[CrossRef](#)]
27. Granados-Reyes, J.; Salagre, P.; Cesteros, Y. Effect of the Preparation Conditions on the Catalytic Activity of Calcined Ca/Al-Layered Double Hydroxides for the Synthesis of Glycerol Carbonate. *Appl. Catal. A Gen.* **2017**, *536*, 9–17. [[CrossRef](#)]
28. Granados-Reyes, J.; Salagre, P.; Cesteros, Y.; Busca, G.; Finocchio, E. Assessment through FT-IR of Surface Acidity and Basicity of Hydrocalumites by Nitrile Adsorption. *Appl. Clay Sci.* **2019**, *180*, 105180. [[CrossRef](#)]
29. Rosset, M.; Perez-Lopez, O.W. Cu–Ca–Al Catalysts Derived from Hydrocalumite and Their Application to Ethanol Dehydrogenation. *React. Kinet. Mech. Catal.* **2019**, *126*, 497–511. [[CrossRef](#)]
30. Souza Júnior, R.L.; Rossi, T.M.; Detoni, C.; Souza, M.M.V.M. Glycerol Carbonate Production from Transesterification of Glycerol with Diethyl Carbonate Catalyzed by Ca/Al-Mixed Oxides Derived from Hydrocalumite. *Biomass Convers. Biorefinery* **2020**. [[CrossRef](#)]
31. Gevers, B.R.; Labuschagné, F.J.W.J. Green Synthesis of Hydrocalumite (CaAl-OH-LDH) from Ca(OH)₂ and Al(OH)₃ and the Parameters That Influence Its Formation and Speciation. *Crystals* **2020**, *10*, 627. [[CrossRef](#)]
32. Fang, L.; Li, W.; Chen, H.; Xiao, F.; Huang, L.; Holm, P.E.; Hansen, H.C.B.; Wang, D. Synergistic Effect of Humic and Fulvic Acids on Ni Removal by the Calcined Mg/Al Layered Double Hydroxide. *RSC Adv.* **2015**, *5*, 18866–18874. [[CrossRef](#)]
33. Li, F.; Kong, Q.; Chen, P.; Chen, M.; Liu, G.; Lv, W.; Yao, K. Effect of Halide Ions on the Photodegradation of Ibuprofen in Aqueous Environments. *Chemosphere* **2017**, *166*, 412–417. [[CrossRef](#)] [[PubMed](#)]
34. Matamoros, V.; Duhec, A.; Albaigés, J.; Bayona, J.M. Photodegradation of Carbamazepine, Ibuprofen, Ketoprofen and 17 α -Ethinylestradiol in Fresh and Seawater. *Water, Air, Soil Pollut.* **2009**, *196*, 161–168. [[CrossRef](#)]
35. Peuravuori, J.; Pihlaja, K. Phototransformations of Selected Pharmaceuticals under Low-Energy UVA-Vis and Powerful UVB-UVA Irradiations in Aqueous Solutions—the Role of Natural Dissolved Organic Chromophoric Material. *Anal. Bioanal. Chem.* **2009**, *394*, 1621–1636. [[CrossRef](#)] [[PubMed](#)]
36. Sá, A.S.; Feitosa, R.P.; Honório, L.; Peña-Garcia, R.; Almeida, L.C.; Dias, J.S.; Brazuna, L.P.; Tabuti, T.G.; Triboni, E.R.; Osajima, J.A.; et al. A Brief Photocatalytic Study of ZnO Containing Cerium towards Ibuprofen Degradation. *Materials* **2021**, *14*, 5891. [[CrossRef](#)] [[PubMed](#)]
37. Da Silva, J.C.C.; Teodoro, J.A.R.; Afonso, R.J.D.C.F.; Aquino, S.F.; Augusti, R. Photolysis and Photocatalysis of Ibuprofen in Aqueous Medium: Characterization of by-Products via Liquid Chromatography Coupled to High-Resolution Mass Spectrometry and Assessment of Their Toxicities against *Artemia Salina*. *J. Mass Spectrom.* **2014**, *49*, 145–153. [[CrossRef](#)]
38. Tian, H.; Fan, Y.; Zhao, Y.; Liu, L. Elimination of Ibuprofen and Its Relative Photo-Induced Toxicity by Mesoporous BiOBr under Simulated Solar Light Irradiation. *RSC Adv.* **2014**, *4*, 13061–13070. [[CrossRef](#)]
39. Li, F.H.; Yao, K.; Lv, W.Y.; Liu, G.G.; Chen, P.; Huang, H.P.; Kang, Y.P. Photodegradation of Ibuprofen under UV-VIS Irradiation: Mechanism and Toxicity of Photolysis Products. *Bull. Environ. Contam. Toxicol.* **2015**, *94*, 479–483. [[CrossRef](#)]
40. Arthur, R.B.; Bonin, J.L.; Ardill, L.P.; Rourk, E.J.; Patterson, H.H.; Stemmler, E.A. Photocatalytic Degradation of Ibuprofen over BiOCl Nanosheets with Identification of Intermediates. *J. Hazard. Mater.* **2018**, *358*, 1–9. [[CrossRef](#)]
41. Akkari, M.; Aranda, P.; Belver, C.; Bedia, J.; Ben Haj Amara, A.; Ruiz-Hitzky, E. ZnO/Sepiolite Heterostructured Materials for Solar Photocatalytic Degradation of Pharmaceuticals in Wastewater. *Appl. Clay Sci.* **2018**, *156*, 104–109. [[CrossRef](#)]
42. Gu, Y.; Yperman, J.; Carleer, R.; D’Haen, J.; Maggen, J.; Vanderheyden, S.; Vanreppelen, K.; Garcia, R.M. Adsorption and Photocatalytic Removal of Ibuprofen by Activated Carbon Impregnated with TiO₂ by UV-Vis Monitoring. *Chemosphere* **2019**, *217*, 724–731. [[CrossRef](#)]
43. Patterson, K.; Howlett, K.; Patterson, K.; Wang, B.; Jiang, L. Photodegradation of Ibuprofen and Four Other Pharmaceutical Pollutants on Natural Pigments Sensitized TiO₂ Nanoparticles. *Water Environ. Res.* **2020**, *92*, 1152–1161. [[CrossRef](#)] [[PubMed](#)]
44. Chopra, S.; Kumar, D. Ibuprofen as an Emerging Organic Contaminant in Environment, Distribution and Remediation. *Heliyon* **2020**, *6*, e04087. [[CrossRef](#)] [[PubMed](#)]
45. Bojer, C.; Schöbel, J.; Martin, T.; Ertl, M.; Schmalz, H.; Brey, J. Clinical Wastewater Treatment: Photochemical Removal of an Anionic Antibiotic (Ciprofloxacin) by Mesostructured High Aspect Ratio ZnO Nanotubes. *Appl. Catal. B Environ.* **2017**, *204*, 561–565. [[CrossRef](#)]
46. Kudo, A.; Miseki, Y. Heterogeneous Photocatalyst Materials for Water Splitting. *Chem. Soc. Rev.* **2009**, *38*, 253–278. [[CrossRef](#)] [[PubMed](#)]
47. Trujillano, R.; Nájera, C.; Rives, V. Activity in the Photodegradation of 4-Nitrophenol of a Zn,Al Hydrotalcite-Like Solid and the Derived Alumina-Supported ZnO. *Catalysts* **2020**, *10*, 702. [[CrossRef](#)]
48. Prince, J.; Tzompantzi, F.; Mendoza-Damián, G.; Hernández-Beltrán, F.; Valente, J.S. Photocatalytic Degradation of Phenol by Semiconducting Mixed Oxides Derived from Zn(Ga)Al Layered Double Hydroxides. *Appl. Catal. B Environ.* **2015**, *163*, 352–360. [[CrossRef](#)]
49. He, S.; Zhang, S.; Lu, J.; Zhao, Y.; Ma, J.; Wei, M.; Evans, D.G.; Duan, X. Enhancement of Visible Light Photocatalysis by Grafting ZnO Nanoplatelets with Exposed (0001) Facets onto a Hierarchical Substrate. *Chem. Commun.* **2011**, *47*, 10797–10799. [[CrossRef](#)]

50. Fan, G.; Li, F.; Evans, D.G.; Duan, X. Catalytic Applications of Layered Double Hydroxides: Recent Advances and Perspectives. *Chem. Soc. Rev.* **2014**, *43*, 7040–7066. [[CrossRef](#)]
51. Di, G.; Zhu, Z.; Zhang, H.; Zhu, J.; Lu, H.; Zhang, W.; Qiu, Y.; Zhu, L.; Küppers, S. Simultaneous Removal of Several Pharmaceuticals and Arsenic on Zn-Fe Mixed Metal Oxides: Combination of Photocatalysis and Adsorption. *Chem. Eng. J.* **2017**, *328*, 141–151. [[CrossRef](#)]
52. Phillips, J.D.; Vandeperre, L.J. Anion Capture with Calcium, Aluminium and Iron Containing Layered Double Hydroxides. *J. Nucl. Mater.* **2011**, *416*, 225–229. [[CrossRef](#)]
53. Lu, Y.; Zhang, Z.; Xu, Y.; Liu, Q.; Qian, G. CaFeAl Mixed Oxide Derived Heterogeneous Catalysts for Transesterification of Soybean Oil to Biodiesel. *Bioresour. Technol.* **2015**, *190*, 438–441. [[CrossRef](#)] [[PubMed](#)]
54. Szabados, M.; Pásztor, K.; Csendes, Z.; Muráth, S.; Kónya, Z.; Kukovecz, Á.; Carlson, S.; Sipos, P.; Pálincó, I. Synthesis of High-Quality, Well-Characterized CaAlFe-Layered Triple Hydroxide with the Combination of Dry-Milling and Ultrasonic Irradiation in Aqueous Solution at Elevated Temperature. *Ultrason. Sonochem.* **2016**, *32*, 173–180. [[CrossRef](#)] [[PubMed](#)]
55. Sánchez-Cantú, M.; Barcelos-Santiago, C.; Gomez, C.M.; Ramos-Ramírez, E.; Ruiz Peralta, M.D.L.; Tepale, N.; González-Coronel, V.J.; Mantilla, A.; Tzompantzi, F. Evaluation of Hydrocalumite-Like Compounds as Catalyst Precursors in the Photodegradation of 2,4-Dichlorophenoxyacetic Acid. *Int. J. Photoenergy* **2016**, *2016*, 5256941. [[CrossRef](#)]
56. Gao, Y.; Zhang, Z.; Wu, J.; Yi, X.; Zheng, A.; Umar, A.; O'Hare, D.; Wang, Q. Comprehensive Investigation of CO₂ Adsorption on Mg-Al-CO₃ LDH-Derived Mixed Metal Oxides. *J. Mater. Chem. A* **2013**, *1*, 12782–12790. [[CrossRef](#)]
57. Jiménez, A.; Vicente, M.A.; Rives, V. Thermal Study of the Hydrocalumite—Katoite—Calcite System. *Thermochim. Acta* **2022**, *713*, 179242. [[CrossRef](#)]
58. Silva, J.M.; Trujillano, R.; Rives, V.; Soria, M.A.; Madeira, L.M. High Temperature CO₂ Sorption over Modified Hydrotalcites. *Chem. Eng. J.* **2017**, *325*, 25–34. [[CrossRef](#)]
59. ICDD Database, JCPDS; International Centre for Diffraction Data (ICDD®): Newtown Square, PA, USA, 2020.
60. Thommes, M.; Kaneko, K.; Neimark, A.V.; Olivier, J.P.; Rodriguez-Reinoso, F.; Rouquerol, J.; Sing, K.S.W. Physisorption of Gases, with Special Reference to the Evaluation of Surface Area and Pore Size Distribution (IUPAC Technical Report). *Pure Appl. Chem.* **2015**, *87*, 1051–1069. [[CrossRef](#)]
61. Lide, D.R. *CRC Handbook of Chemistry and Physics*, 76th ed.; CRC Press: Boca Raton, FL, USA, 1995.
62. Cavani, F.; Trifirò, F.; Vaccari, A. Hydrotalcite-Type Anionic Clays: Preparation, Properties and Applications. *Catal. Today* **1991**, *11*, 173–301. [[CrossRef](#)]
63. López-Salinas, E.; Serrano, M.E.L.; Jácome, M.A.C.; Secora, I.S. Characterization of Synthetic Hydrocalumite-Type [Ca₂Al(OH)₆]NO₃·mH₂O: Effect of the Calcination Temperature. *J. Porous Mater.* **1996**, *2*, 291–297. [[CrossRef](#)]
64. Radha, A.V.; Kamath, P.V.; Shivakumara, C. Mechanism of the Anion Exchange Reactions of the Layered Double Hydroxides (LDHs) of Ca and Mg with Al. *Solid State Sci.* **2005**, *7*, 1180–1187. [[CrossRef](#)]
65. Rousselot, I.; Taviot-Guého, C.; Leroux, F.; Léone, P.; Palvadeau, P.; Besse, J.P. Insights on the Structural Chemistry of Hydrocalumite and Hydrotalcite-like Materials: Investigation of the Series Ca₂M³⁺(OH)₆Cl·2H₂O (M³⁺: Al³⁺, Ga³⁺, Fe³⁺, and Sc³⁺) by X-ray Powder Diffraction. *J. Solid State Chem.* **2002**, *167*, 137–144. [[CrossRef](#)]
66. Pérez-Barrado, E.; Pujol, M.C.; Aguiló, M.; Cesteros, Y.; Díaz, F.; Pallarès, J.; Marsal, L.F.; Salagre, P. Fast Aging Treatment for the Synthesis of Hydrocalumites Using Microwaves. *Appl. Clay Sci.* **2013**, *80–81*, 313–319. [[CrossRef](#)]
67. Jenkins, R.; de Vries, J.L. Worked Examples in X-ray Analysis. In *Part of the Philips Technical Library Book Series*; Springer: Berlin, Germany, 1978.
68. Nyquist, R.A.; Kagel, R.O. *Infrared Spectra of Inorganic Compounds*; Academic Press: New York, NY, USA, 2001.
69. Bastida, J.; Bolós, C.; Pardo, P.; Serrano, F.J. Análisis Microestructural Por DRX de CaO Obtenido a Partir de Carbonato Cálcico Molido (CCM). *Bol. Soc. Esp. Cerám. Vidr.* **2004**, *43*, 80–83. [[CrossRef](#)]
70. Pan, X.; Liu, J.; Wu, S.; Yu, H. Formation Behavior of Tricalcium Aluminate Hexahydrate in Synthetic Sodium Aluminate Solution with High Alkali Concentration and Caustic Ratio. *Hydrometallurgy* **2020**, *195*, 105373. [[CrossRef](#)]
71. Nakamoto, K. *Infrared and Raman Spectra of Inorganic and Coordination Compounds: Part A: Theory and Applications in Inorganic Chemistry*; Wiley: Hoboken, NJ, USA, 2008.
72. Granados-Reyes, J.; Salagre, P.; Cesteros, Y. Effect of Microwaves, Ultrasounds and Interlayer Anion on the Hydrocalumites Synthesis. *Micropor. Mesopor. Mater.* **2014**, *199*, 117–124. [[CrossRef](#)]
73. Domínguez, M.; Pérez-Bernal, M.E.; Ruano-Casero, R.J.; Barriga, C.; Rives, V.; Ferreira, R.A.S.; Carlos, L.D.; Rocha, J. Multiwavelength Luminescence in Lanthanide-Doped Hydrocalumite and Mayenite. *Chem. Mater.* **2011**, *23*, 1993–2004. [[CrossRef](#)]
74. Chen, G.; Qian, S.; Tu, X.; Wei, X.; Zou, J.; Leng, L.; Luo, S. Enhancement Photocatalytic Degradation of Rhodamine B on NanoPt Intercalated Zn-Ti Layered Double Hydroxides. *Appl. Surf. Sci.* **2014**, *293*, 345–351. [[CrossRef](#)]
75. Padilla Villavicencio, M.; Escobedo Morales, A.; de Ruiz Peralta, M.L.; Sánchez-Cantú, M.; Rojas Blanco, L.; Chigo Anota, E.; Camacho García, J.H.; Tzompantzi, F. Ibuprofen Photodegradation by Ag₂O and Ag/Ag₂O Composites Under Simulated Visible Light Irradiation. *Catal. Lett.* **2020**, *150*, 2385–2399. [[CrossRef](#)]

76. Liu, S.H.; Tang, W.T.; Chou, P.H. Microwave-Assisted Synthesis of Triple 2D g-C₃N₄/Bi₂WO₆/RGO Composites for Ibuprofen Photodegradation: Kinetics, Mechanism and Toxicity Evaluation of Degradation Products. *Chem. Eng. J.* **2020**, *387*, 124098. [[CrossRef](#)]
77. Miranda, M.O.; Cabral Cavalcanti, W.E.; Barbosa, F.F.; Antonio De Sousa, J.; Ivan Da Silva, F.; Pergher, S.B.C.; Braga, T.P. Photocatalytic Degradation of Ibuprofen Using Titanium Oxide: Insights into the Mechanism and Preferential Attack of Radicals. *RSC Adv.* **2021**, *11*, 27720–27733. [[CrossRef](#)]